



HAL
open science

3-D High Frame Rate Imaging With Motion Compensation (3-D HFR With MoCo): An Experimental Evaluation

Sebastien Salles, François Varray, Damien Garcia, Hervé Liebgott, Barbara Nicolas

► **To cite this version:**

Sebastien Salles, François Varray, Damien Garcia, Hervé Liebgott, Barbara Nicolas. 3-D High Frame Rate Imaging With Motion Compensation (3-D HFR With MoCo): An Experimental Evaluation. IEEE Open Journal of Ultrasonics, Ferroelectrics, and Frequency Control, 2023, 3, pp.137-145. 10.1109/OJUFFC.2023.3308486 . hal-04273519

HAL Id: hal-04273519

<https://hal.science/hal-04273519>

Submitted on 2 Feb 2024

HAL is a multi-disciplinary open access archive for the deposit and dissemination of scientific research documents, whether they are published or not. The documents may come from teaching and research institutions in France or abroad, or from public or private research centers.

L'archive ouverte pluridisciplinaire **HAL**, est destinée au dépôt et à la diffusion de documents scientifiques de niveau recherche, publiés ou non, émanant des établissements d'enseignement et de recherche français ou étrangers, des laboratoires publics ou privés.



Distributed under a Creative Commons Attribution 4.0 International License

3-D high frame rate imaging with motion compensation (3-D HFR with MoCo): an experimental evaluation

Sebastien Salles^{1,2}, François Varray³, Damien Garcia³, Hervé Liebgott³, Barbara Nicolas³

¹Sorbonne Université, CNRS, INSERM, Laboratoire d'Imagerie Biomédicale, LIB, Paris, F-75006, FR. ²Norwegian University of Science and Technology, ISB, Trondheim, Trøndelag, NO. ³Univ Lyon, INSA-Lyon, Université Claude Bernard Lyon 1, UJM-Saint Etienne, CNRS, Inserm, CREATIS UMR 5220, U1206, F-69621, LYON, France

Abstract—Improving the image quality of 3D high-frame-rate (HFR) echocardiography has become an important research focus.

Diverging Waves techniques have already shown promising results in 3D ultrasound imaging. However, phase delays induced by large tissue displacements between ultrasound transmission can deteriorate the compounding process. Motion compensation (MoCo) approaches have been introduced and integrated into the compounding process in 2-D and in 3-D simulated ultrasound volume. Here, we propose to investigate the influence of the MoCo approach on different scenarios, including several 3-D diverging wave strategies and configurations of virtual sources. First, we proposed to formalize the placement of virtual sources according to different scenarios. Then the proposed method has been tested on numerical simulations using Field II, and in vitro experimentations with a homemade rotating phantom. The nine approaches were compared quantitatively by estimating the contrast to noise (CNR) and contrast ratio (CR). The results confirmed that MoCo increased the CNR and CR for each case. On average, the MoCo algorithm increased the CNR/CR by +3.2/8.4 dB *in silico*, and of +1.4/1.8 dB *in vitro*, respectively

Keywords— Ultrafast Imaging, Motion Compensation, Diverging Waves, Cardiac imaging, 3-D, Echocardiography

I. INTRODUCTION

Over the last few years, 3-D ultrasound imaging has undergone important technical improvements that enable the implementation of 3-D high frame rate (HFR) imaging on both research and clinical scanners. By improving the temporal resolution, 3-D HFR allows for the study of very fast phenomena such as blood flow in the heart [1], arteries [2], and brain [3] or the propagation of natural mechanical waves occurring in the myocardium and along vessels walls [4]–[7]. In the past decade, research has focused on developing new acquisition schemes enabling 3-D ultrasound imaging with higher temporal resolution. The 3-D extension of a radar-based technique, called synthetic aperture, is one of the most promising solutions. Synthetic aperture imaging consists of coherently combining low-quality images obtained at the pulse repetition frequency (PRF) without transmit focusing into one single final image of high quality. This technique allows ultrasound imaging at high frame rate (500 to 10 000 frames/s) while keeping sufficient image quality. The compromise between the frame rate and image quality depends on the application. Plane or diverging waves are commonly transmitted. Montaldo *et al.* used multiple plane waves

emitted from different angles and summed the backscattered signals coherently to form a high-quality final images [8]. Papadacci *et al.* used diverging waves to obtain high-frame-rate imaging of the heart [9]. In both methods, low-resolution images from different insonification angles are summed together to provide synthetic aperture imaging. The multi-line transmit (MLT) approach is another technique able to reach high-frame-rate imaging. Here the gain of time is obtained by simultaneously transmitting several focused transmissions in different directions instead of a single focused beam [10]. The 3D extensions of both methods have been achieved in multiple applications, such as vascular and cardiac imaging [11]–[13].

Diverging wave imaging is obtained by locating several virtual sources behind the probe. The virtual source positions can be set according to the required ultrasound steering angle while keeping the sub-aperture unchanged. On the other hand, the virtual sources can be placed by keeping the steering angle unchanged, while sliding the sub-aperture along the transducer.

In cardiac imaging, large tissue displacements can occur between ultrasound transmissions, which may induce significant phase delays between successive transmissions. Phase delays between the transmissions make the compounding process not fully coherent, which leads to the deterioration of the image quality. Inspired by synthetic aperture radar [14], several approaches were proposed to offset tissue motion in synthetic aperture ultrasound imaging [15]–[18]. In a more recent paper, Dénarié *et al.* [19] demonstrated, in a rat heart, the benefits of motion compensation for coherent plane-wave imaging, and Porée *et al.* [20] introduced a motion compensation (MoCo) approach that compensated for the tissue motion within the compounding process and demonstrated its benefits in the human heart. Using Block-Matching compensation technique, Nie *et al.* have shown a contrast enhancement in 2D [21]. The 3-D HFR with MoCo approach was recently tested in simulation by comparing the results obtained with diverging waves (with sliding sub-apertures) and MLT approach [22]. By estimating and compensating the motion in 3-D, Chen *et al.* showed the benefits of motion compensation in 3D [23]. Moreover, the feasibility of 3-D HFR with MoCo was validated experimentally [24].

This work aims to investigate the influence of 3-D HFR with MoCo approach on three synthetic aperture strategies with three configurations of virtual sources. First, the locations of the virtual sources were formalized according

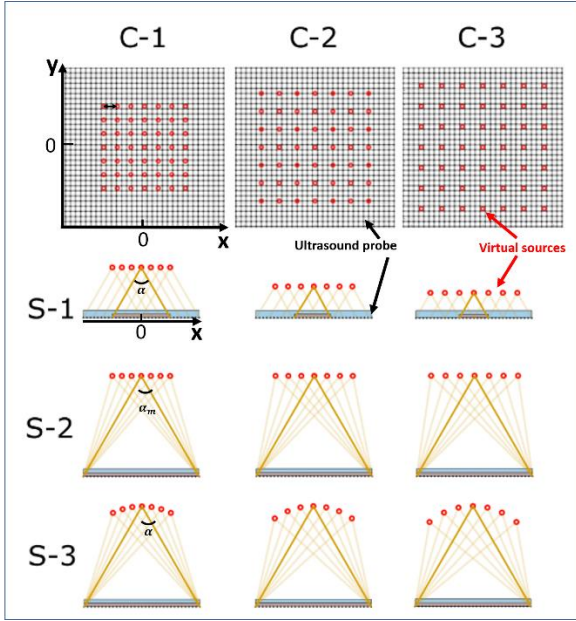


Figure 1: 2D representation of the nine different 3D transmission strategies used in this manuscript with $N_x=N_y=7$ elements. The three virtual sources configurations C-1, C-2, and C-3 are depicted on top of the 2D probe. S-1, S-2, and S-3 correspond to the three strategies used in this manuscript. α is the chosen opening angle for the strategies S-1 and S-3. α_m is the chosen opening angle of the diverging waves strategy S-2.

to the chosen diverging wave strategy and the diverging wave opening angle. Then, the nine approaches were compared quantitatively by estimating the CNR and CR, on both simulated and experimental data. The presented 3-D HFR with MoCo method with different DW transmission strategies was tested using a single simulation realization in a conference paper [25]. Here, we evaluated the nine approaches on five simulation realizations including noise analysis. The originality of this work is also found in the evaluation of 3-D HFR with MoCo *in vitro*. Indeed, this work presents results obtained on a homemade disk rotating at different speeds by using an advanced platform composed of 4 synchronized Vantage systems.

II. MATERIAL AND METHOD

A. 3-D Diverging waves strategies

In this work, three diverging wave strategies [S-1, S-2, and S-3, Figure 1] were analyzed. Three configurations of virtual sources were considered [C-1, C-2, C-3] for each strategy.

The first strategy (S-1) consisted in transmitting 3-D diverging waves with sub-apertures sliding according to the position of the virtual sources [22]. The axial position of the virtual sources vs_z was defined as follows:

$$S-1 : vs_z = \frac{N_{x,y} \times pitch_{x,y}}{2 \times D \times \tan(\alpha/2)}, \quad (1)$$

where $N_{x,y}$ is the number of elements in each direction, $pitch_{x,y}$ are the distances between each ultrasound probe element in each direction, the constant D stands for the ratio between the size of the chosen sub-

aperture and the size of the full aperture, and α is the chosen opening angle of the diverging wave.

The second scenario (S-2) aimed to transmit diverging waves with the entire aperture. The axial position of the virtual sources vs_z was defined as follows:

$$S-2 : vs_z = \frac{N_{x,y} \times pitch_{x,y}}{2 \times \tan(\alpha_m/2)} \quad (2)$$

where α_m is the chosen opening angle of the diverging wave, at the probe center. Note that the virtual sources were positioned in a plane parallel to the probe for the S-1 and S-2 scenarios. As a result, the opening angles of the diverging waves varied slightly from one transmission to another for the strategies S-2.

The third scenario (S-3) also transmits the 3-D diverging waves with the full aperture. However, in this case the virtual sources were placed on a spherical surface which allows the aperture angle to be kept constant from one transmission to the next. The virtual source z-position vs_z was defined as follows:

$$S-3 : vs_z(i, j) = \sqrt{\frac{\pi \times (N_{x,y} \times pitch)^2}{4 \times \alpha} - vs_x^2(i, j) - vs_y^2(i, j)} \quad (3)$$

where α is the chosen opening angle of the diverging waves, and, vs_x and vs_y are the lateral and elevational coordinates of the virtual sources

In this work, we formalized a uniform distribution of virtual sources according to the numbers of virtual sources N_s using a parameter D. The lateral x and elevational y coordinates of the virtual sources have been defined from the strategies S-1. Regarding strategy S-1, the position of the virtual sources (and thus the virtual pitch, which is the distance in x and y between the virtual sources), depends on the size of the sub-aperture. Hence the virtual pitch (Eq 6) has been defined according to the ratio D. In order to accomplish a fair comparison, the same lateral and elevation position of the virtual sources have been used for the strategies S-2 and S-3.

Note that in strategies S-2 and S-3, since the full aperture is used, the notion of sub-aperture does not hold

Assuming a 2D matrix probe, the lateral and elevational coordinates of the virtual sources, vs_x and vs_y were defined as follows:

$$vs_x(i, j) = \frac{N_x \times (1-D)}{2 \times D} \times pitch_x + (i-1) \times Vpitch_x, \quad (4)$$

$$i: \{1, 2, \dots, \sqrt{N_s}\}, j: \{1, 2, \dots, \sqrt{N_s}\}$$

and

$$vs_y(i, j) = \frac{N_y \times (1-D)}{2 \times D} \times pitch_y + (j-1) \times Vpitch_y, \quad (5)$$

$$i: \{1, 2, \dots, \sqrt{N_s}\}, j: \{1, 2, \dots, \sqrt{N_s}\}$$

where N_s is the number of virtual sources, $Vpitch_{x,y}$ are the virtual pitches and correspond to the distances between two virtual sources in each direction defined as follows

$$Vpitch_{x,y} = N_{x,y} \times \frac{(D-1)}{D \times (\sqrt{N_s} - 1)} \times pitch_{x,y} \quad (6)$$

The three different virtual source configurations C-1, C-2, and C-3 were defined according to the values of D (2, 3, 4).

B. Proposed 3-D HFR with MOCO strategy

A “round-trip” scan sequence was achieved to perform MoCo (Figure 2) [22]. The virtual sources (i.e., the black spots) were sequentially activated from the start point to the endpoint (indicated by the arrows in Figure 2), and then from the endpoint to the start point. Hence, 49 transmissions (7×7 virtual sources) were computed to reconstruct one volume.

The radial motion was estimated with two lag-one auto correlations along the slow-time axis, both corresponding to the forward and backward path, respectively. For M with (M even) transmissions, the autocorrelation was given by:

$$\mathfrak{R}_1 = \sum_{m=1}^{M/2-1} \frac{\widetilde{s}_m \widetilde{s}_{m+1}}{|\widetilde{s}_m \widetilde{s}_{m+1}|} \quad (7)$$

$$\mathfrak{R}_2 = \sum_{m=M/2}^{M-1} \frac{\widetilde{s}_m \widetilde{s}_{m+1}}{|\widetilde{s}_m \widetilde{s}_{m+1}|} \quad (8)$$

where, \widetilde{s}_m are the slow-time IQ samples. The phase delays ϕ due to radial motion \hat{V} were estimated using the phase angle of the $\mathfrak{R}_1 \mathfrak{R}_2$ product:

$$\phi = \frac{\angle \mathfrak{R}_1 \mathfrak{R}_2(1)}{2}, \quad (9)$$

and

$$\hat{V} = \frac{\phi}{\pi} \times vNyq, \quad (10)$$

with

$$vNyq = \frac{C_0 \times PRF}{4f_0}, \quad (11)$$

where C_0 is the sound speed, PRF the pulse repetition frequency, and f_0 the central probe frequency. Note that each autocorrelations have been spatially smoothed using a spatial averaging windows of $8.1 \times 8.1 \times 11$ mm ($20 \times 20 \times 20$ pixels, found empirically) in x, y, and z directions

As demonstrated in [20], this round-trip double autocorrelation technique eliminates the artifacts due to side lobes. The motion is then compensated by adjusting the frame-to-frame displacement and phase rotation before the compound process, assuming a constant motion between the first and the last transmission. For more details and in order to make our work reproducible, the 3D MOCO algorithm and one simulated dataset are available here: https://www.creatis.insa-lyon.fr/3D_HFR_with_MOCO/

C. Simulation and Experimental Setup

• Simulation Setup

A matrix transducer made of 32-by-32 elements with a 3 MHz center frequency was simulated with Field II [26], [27]. The simulation information is summarized in Table 1. In the beamforming process, the pulse repetition frequency (PRF) was set to 4 kHz. 2D Hanning window was applied in transmit.

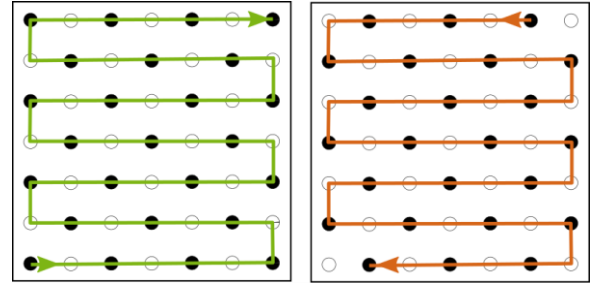


Figure 2: MOCO strategy. The green arrow indicates the forward path, and the brown arrow indicates the backward path. The black spots indicate the activated virtual sources in the round-trip scan sequence. In total 49 transmissions (7×7) were performed

The imaging object was a 40 mm \times 40 mm \times 40 mm (lateral \times elevation \times axial) cubic phantom containing a spherical cystic region with a radius of 10 mm. $5/\text{mm}^3$ scatters density has been used. The scattering amplitudes were randomly distributed between 0 and 1 following a uniform distribution outside the cystic region and set to 0 inside the cystic region. The performance of the proposed MoCo strategies was investigated by moving the phantom in the axial direction at a speed of 10 cm/s. The simulations were performed 5 times for each case.

Table 1 FIELD II simulation parameters

Transducer configuration	
Number of elements	32 \times 32
Central probe frequency	3 MHz
Element size	0.3 \times 0.3 mm
Bandwidth	0.6
Pulse length	1.5 cycles
Simulation Setup	
Speed of sound	1 540 m/s
Sampling frequency	25 MHz
Pulse repetition frequency	4 kHz
Apodization function in transmit	Hanning window
Apodization function in receive	None

• Experimental Setup

All experimental measurements were performed with a 2.97 MHz 1024-element cardiac ultrasound probe (Vermon, Tours, France) driven by 4 individual Vantage 256 systems (Verasonics, Kirkland, WA, USA) [28] synchronized together. A 2D Hanning apodization was introduced in transmission. The IQ signals were

beamformed using a delay-and-sum and the full receive aperture. The volume was reconstructed with an opening angle of 60° by 60° .

The 3-D HFR with MoCo approach was tested on a 10-cm-diameter agar-agar tissue-mimicking spinning disk. The center was placed 15 cm away from the probe. The tissue-mimicking phantom was made using a similar recipe to that described in [29]. Four equidistant 0.8 cm diameter anechoic cysts were located at 2.5 cm from the disk center (Figure 3). This disk was mounted on a step motor assembly allowing control of its rotational speed. Hence, the setup produced a 2D motion in a 3D phantom. These experiments were conducted with 4 angular velocities (0, 0.837 1.67 and 2.51 rad/s), which gave a maximum outer speed of 12.56 cm/s. The contrast-ratio (CR) and contrast-to-noise-ratio (CNR) measurements were performed on the four anechoic regions and only the average values are shown in this paper.

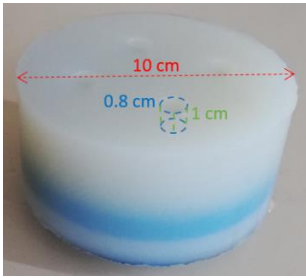


Figure 3: 3-D experimental imaging object. The imaging object was a 10-cm-diameter agar-agar tissue-mimicking spinning disk, containing four equidistant 0.8 cm diameter anechoic cysts.

- *Comparison metrics*

To investigate the performance of the proposed 3-D MoCo strategies, we calculated the CNR and the CR of the anechoic regions :

$$CNR = 20 \times \log_{10} \left(\frac{\mu_{back} - \mu_{cyst}}{\sqrt{\sigma_{back}^2 + \sigma_{cyst}^2}} \right) \quad (8)$$

$$CR = \mu_{back} - \mu_{cyst} \quad (9)$$

Where μ_{back} and μ_{cyst} were the average image intensities (after log-compression) outside and inside the cystic regions, respectively. σ_{back} and σ_{cyst} were their respective standard deviations (Figure 4).

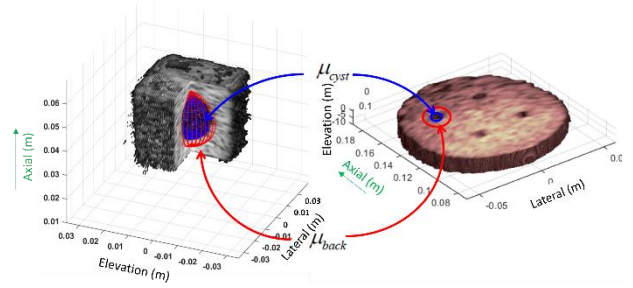


Figure 4: Illustrations of imaging object and quantitative analysis of contrast ratio (CR) and contrast-to-noise ratio (CNR). a. In simulation, the sphere in blue is defined as the cystic region (radius: 10 mm), while the spherical shell in red is defined as the background region (inner radius: 11 mm, outer radius: 13 mm). b. In the experiment, the cylinder in blue is defined as the cystic region (4 mm radius), while the cylindrical shell in blue is defined as the background region (5 mm inner radius, 6.5mm outer radius, 5 mm depth).

Furthermore, in order to test the robustness of the proposed techniques to noise at different signal-to-noise ratio (SNR) levels, noise was added in the simulations after the beamforming process and before MoCo. Note that the speckle region has been used as the signal.”

III. RESULTS

A. Simulation results

An example of the results obtained in simulation with the C-1 virtual sources configurations and S-1 diverging wave strategy is shown in Figure 5. Figure 5a shows the results without motion compensation containing noticeable

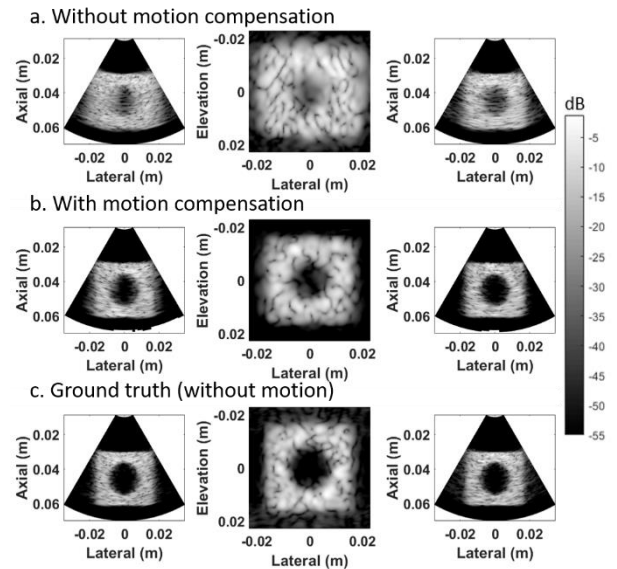


Figure 5: Volume obtained with the diverging waves strategy S-1 and the C-1 virtual sources configuration in simulation. The 1st column shows the lateral-axial plane, the 2nd column the C-plane view at a depth of 50 mm the 3rd column the elevation-axial plane. (a) Images acquired in the moving state without MoCo with motion in the axial direction at a velocity of 10 cm/s. (b) Images acquired in the moving state with MoCo. (c) Images acquired in without any motion.

motion artifacts and resulting in blurry and low image

quality. The image Figure 5b depicts the results with motion compensation qualitatively showing the restored motion and image quality.

The CRs and CNRs of the nine strategies are summarized in Figure 6. The boxes in yellow/gray colors indicate the results without/with MoCo, respectively. On average, the motion compensation algorithm increased for the S-1, S-2, and S-3 strategies, the CR of 9.62 ± 0.25 , 8.56 ± 0.49 and 6.77 ± 0.34 , in dB, respectively, and the CNR of 3.8 ± 0.23 , 2.56 ± 0.22 , and 3.17 ± 0.16 , in dB, respectively.

Regarding the results without motion compensation, all the configurations and strategies had low CNR below 5 dB. The diverging wave strategies S-3 showed slightly higher CNR for the three virtual source configurations (C-1, C-2, and C-3). No consistent trends were found for CR results. When motion compensation was applied, the CNR and CR increased for all strategies and configurations. The diverging wave strategy S-1 showed slightly higher CR and CNR for the three virtual source configurations.

Moreover, the virtual sources configuration C-3 combined with S-1 (corresponding to the smaller sub-aperture) gave slightly higher CNR than C-2 and C-1.

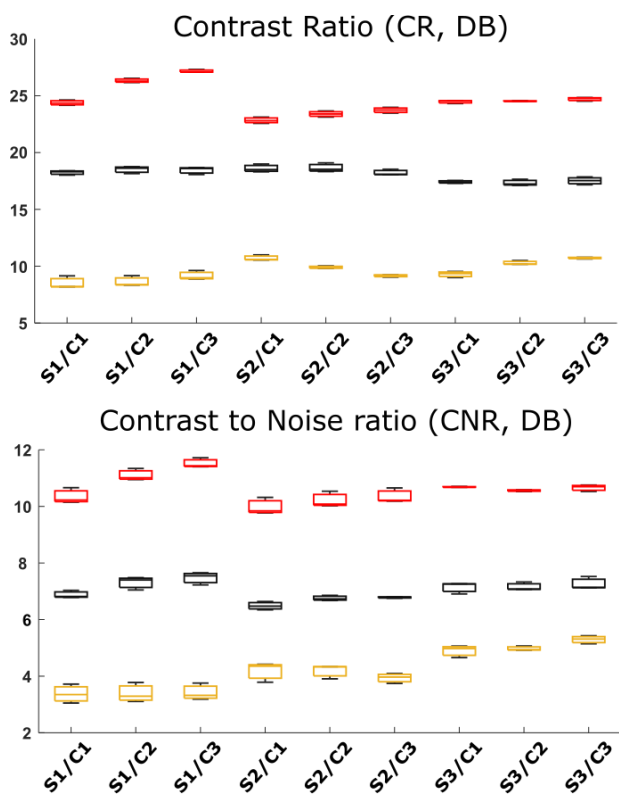


Figure 6 Quantitative CNRs and CRs of the S-1, S-2, and S-3 diverging wave strategies with the three virtual source configurations (C-1, C-2, and C-3) being tested in simulation. Five simulations were achieved for each case. The boxes in yellow/black colors indicate the results without/with MoCo with motion in the axial direction at a velocity of 10 cm/s, respectively. The red boxes indicate the results in the motionless state, shown as a benchmark. On each box, the central mark indicates the average, and the bottom and top edges of the box indicate the 25th and 75th percentiles,

respectively. The whiskers extend to the most extreme data points

The quantitative CRs and CNRs of each transmission strategy at different SNR levels are presented in Figure 7. To better appreciate the results, only the average value over the 3 virtual source configurations and the 5 simulations are depicted. 3-D HFR with MoCo showed higher CNRs and CRs in all SNR conditions and for each transmission strategy. Interestingly, taking into account the tissue motion in the beamforming process enabled us to keep high CR and CNR until the SNR became smaller than 35 dB. In contrast, CR and CNR were much lower when motion was not compensated, especially in the presence of noise. Note that the discontinuity around 20dB is due to insufficient speckle/noise realization

B. Experimental results

An example of the results obtained with the C-1 virtual sources configurations and S-1 diverging wave strategy for three rotation speeds is shown in Figure 8. In Figure 8A, the 1st column shows the results without motion compensation containing noticeable motion artifacts. The 2nd column depicts the results with motion compensation, qualitatively showing the restored anechoic cysts and image quality. The 3rd column shows the corresponding tissue Doppler estimation. Figure 8B shows one anechoic region (green rectangle) comparison between the results obtained without and with MoCo. Finally, Figure 8C shows the phantom image in the static state, which is taken as a benchmark. Qualitatively, without the MoCo strategies, image quality decreased with increasing speed. On the other hand, similar results were obtained with the three different rotation speeds when the MoCo strategy was employed.

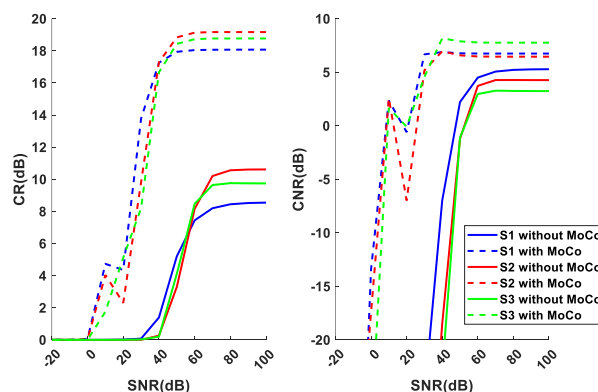


Figure 7 The average CNRs and CRs values over the three different virtual source configurations for the three diverging wave strategies (S1, S2 and S3) in the presence of different levels of noise.

The nine strategies' average CNRs and CRs over the three rotation speeds are summarized in Figure 9. The boxes in yellow/gray colors indicate the results without/with MoCo, respectively. On average, the motion compensation algorithm increased, for the S-1, S-2, and S-3 strategies, the CNR of 1.28 ± 0.57 , 1.58 ± 0.74 , and 1.47

± 0.68 dB, respectively, and the CR of 1.58 ± 0.74 , 1.64 ± 0.88 , and 2.2 ± 0.46 dB, respectively.

Regarding CR, with and without motion compensation, the three different strategies gave very similar results. However, the virtual sources configuration C1 showed higher CR for the three different strategies (S-1, S-2, and S-3). Regarding CNR, the virtual sources C-1 also showed higher values for the three different strategies. Moreover, the strategy S-3 showed slightly higher CNR compared to the others (Figure 9).

Figure 10 depicts the average CNRs and CRs of the three strategies over three virtual sources configuration. Concerning the CR, the same strategies tendency was found at each rotation speed, with the strategy S2 slightly worse than the two others. No difference was visible between each rotation speed. The CNR measurement results showed decreasing image quality with increasing rotation speed for both with and without MoCo.

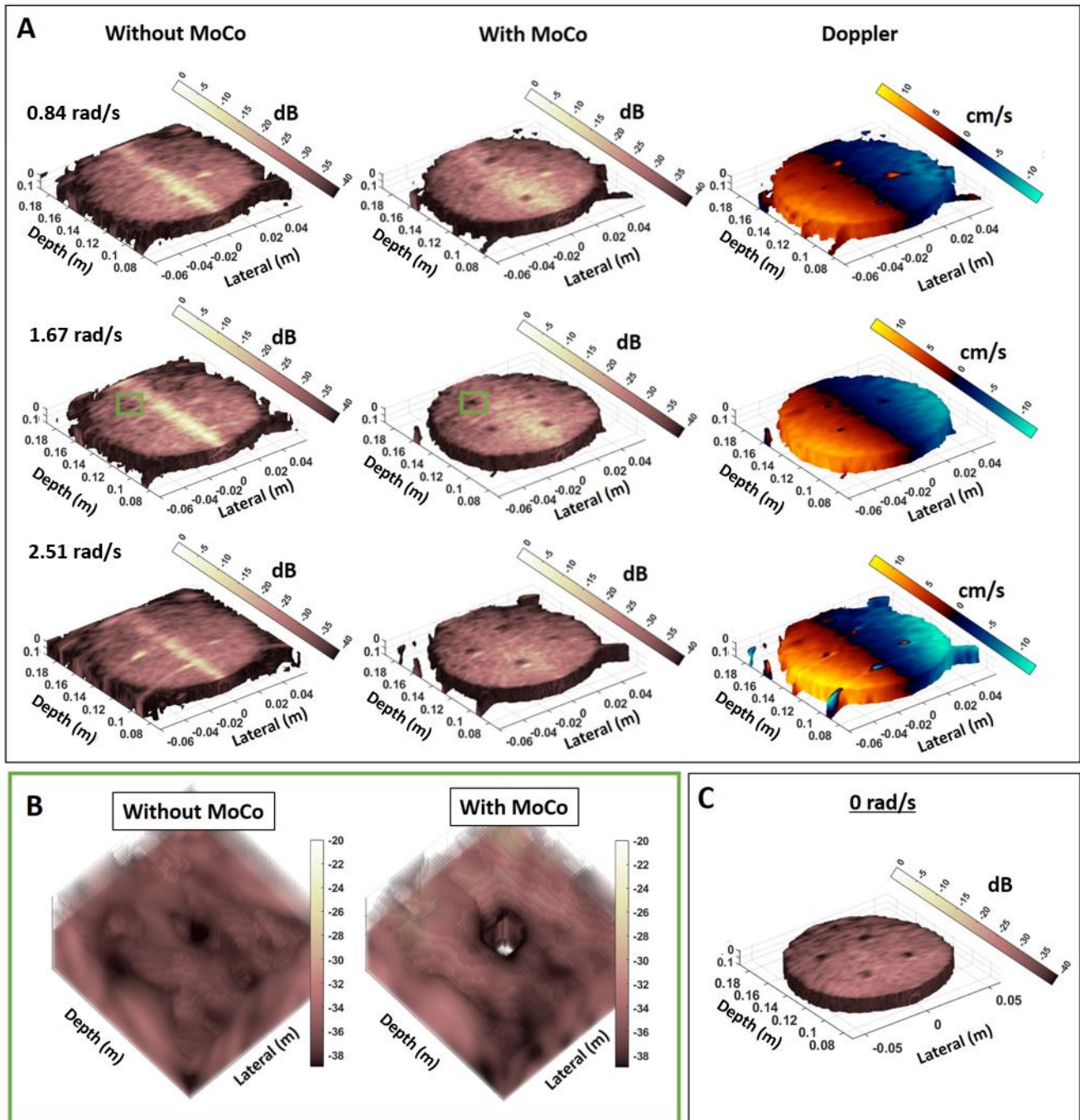


Figure 8 Volume obtained with the diverging waves strategy S-1 and the C-1 virtual sources configuration. In A, the 1st column shows the volume acquired in the moving state without MoCo, the 2nd column shows the volume acquired in the moving state with, the 3rd column shows MoCo the estimated Doppler velocity. The first, second, and third row show the results obtain with 0.837 1.67 and 2.51 rad/s, respectively, the green rectangle depicted the Region of interest taken in B. B shows one anechoic region comparison between the results obtain without and with MoCo. C shows the volume acquired in a static state. In order to better appreciate the 3D rendering, the results were masked by only keeping the voxel amplitude superior to -40 dB.

IV. DISCUSSION / CONCLUSIONS

In this work, we evaluated the influence of a 3-D HFR with MoCo approach on three different 3-D diverging wave strategies with three different configurations of virtual sources in simulation and in experimentation. The major conclusions of this study are: i) the 3-D HFR with MoCo approach is recommended for all velocities tested which were all superior to 8 cm/s (corresponding to the speed of the cyst at 4kHz), ii) the use of a small virtual pitch (V_{pitch} , Eq 3) gives slightly better CR and CNR, in experimentation. The positions of the virtual sources were formalized according to the chosen diverging waves strategy and the diverging waves opening angle. Even if only three 3-D diverging wave strategies were tested in this study, those are the most straightforward and used strategies in the ultrasound community [4], [6], [11], [30]. Other 3-D ultrasound approaches, called 3D multi-line transmit (MLT) and Multi-Plane-Transmit beamforming [22], [31]–[33], and showing convincing results, were not evaluated in this study.

Because the influence of 3-D HFR with MoCo strategies has already been studied in simulation [22] by showing slightly better results with a diagonal round-trip, only one MoCo strategy was used in the study. In this work, the parallel round-trip has been chosen empirically.

First, the influence of a 3-D HFR with MoCo over the different approaches was evaluated quantitatively by estimating the CNR, and CR in simulation. Even if the nine strategies gave very similar results, the diverging wave strategies S-1 combined with the C-3 virtual sources configuration seems to be the best compromise in simulation.

It is important to note that the acquisition schemes will affect both the image quality and the motion estimation itself. For instance, in Figure 6, the strategy S-3 has a better CNR than the strategy S-1 with motion (yellow box) but have a lower CNR than strategies S-1 without motion (red box). This may indicate that the strategy S-3 is more robust to motion due to a larger volume ofinsonification. Moreover, when motion correction is applied the strategy S-1 has better CNR than the strategy S-3, especially with the C-3 virtual sources. This may indicate a better motion estimation and correction due to a larger field of view induced by the use of a smaller sub-aperture.

The results confirmed that MoCo increased the CNR and CR for each case. On average, the motion compensation algorithm increased for the S-1, S-2, and S-3 strategies, the CR of 9.62 ± 0.25 , 8.56 ± 0.49 and 6.77 ± 0.34 , in dB, respectively, and the CNR of 3.8 ± 0.23 , 2.56 ± 0.22 , and 3.17 ± 0.16 , in dB, respectively. By comparing the CNR and CR value obtained in this study to those presented in [22] differences can be noticed. Indeed, the CNR and CR values measured in [22] are two times higher than those presented in this manuscript, for an similar simulation setup. This difference can be explained by the way the ROIs are defined especially the size of the gap between the regions inside and outside of the cyst. Indeed, there is more leakage close to the limit of the cyst, decreasing in our case the contrast values, since we defined the limits close to the actual cyst values. That said, the most important is probably to analyze the improvement qualitatively since the metrics and configurations are not similar. In the

present study, we chose the inside region of interest (μ_{cyst} , Figure 4) as close as possible of the cyst size to better take into account the cyst edge effect.

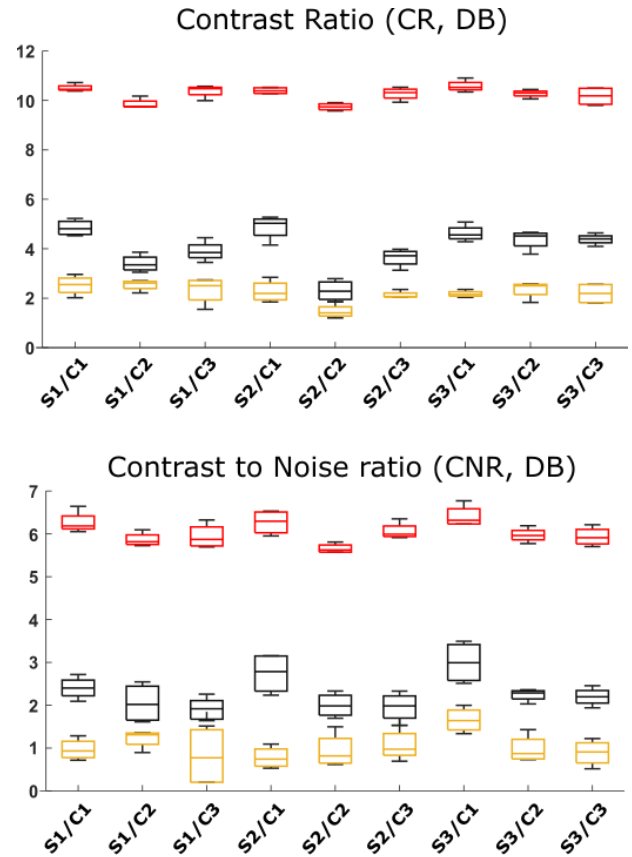


Figure 9: Quantitative average CNRs and CRs, in dB, of the S-1, S-2, and S-3 diverging wave strategies with the three virtual sources configuration (C-1, C-2, and C-3), over the three rotation speeds, being tested in experiments. The bars in yellow/black colors indicate the results without/with MoCo, respectively. The red lines indicate the results in the static state, shown as benchmark. On each box, the central mark indicates the average, and the bottom and top edges of the box indicate the 25th and 75th percentiles, respectively. The whiskers extend to the most extreme data points.

Contrary to the simulation setup where three virtual source confirmations gave very similar results, the C-1 configuration (smaller virtual pitch) exhibited better results in terms of CNR and CR for each strategy.

The difference in terms of cyst localization and the phantom velocity between the simulation data and of the experimental data can help to explain the differences. Indeed, the cyst is located in the middle of the ultrasound field for the simulation data set where there are close to the extremity for the experimentation. Moreover, in the simulation, the phantom is moving along the depth only, whereas the experimental results show a rotating disc. Knowing that the presented algorithms only correct for axial motion, the lateral motion of the rotating disk is not corrected. Regarding the average value over the 3 rotation speeds (Figure 9) the strategies S-1 and S-3 combined with C-1 configuration gave slightly better results in terms of CR and CNR, respectively. For the strategies S-1, the smallest virtual pitch generates the highest acoustic energy which, from an experimental point of view, may explain

the better results in terms of CR and CNR obtained with the configuration C-1. For the strategy S-3 the use of a smaller virtual pitch induces a smaller transmission angle.

In terms of image quality, the use of a too-large transmission angle could deteriorate the coherent summation of the received echo with motion. In terms of motion estimation, according to the literature, the use of a larger transmission angle should increase the 2D motion estimation quality [34]. This is not the case in the presented results (Figure 9) where the CNR and CR without MoCo (yellow box) follow the same evolution as those with MoCo (black box) and without motion (red box). This can be explained by the fact that only the axial motion is estimated.

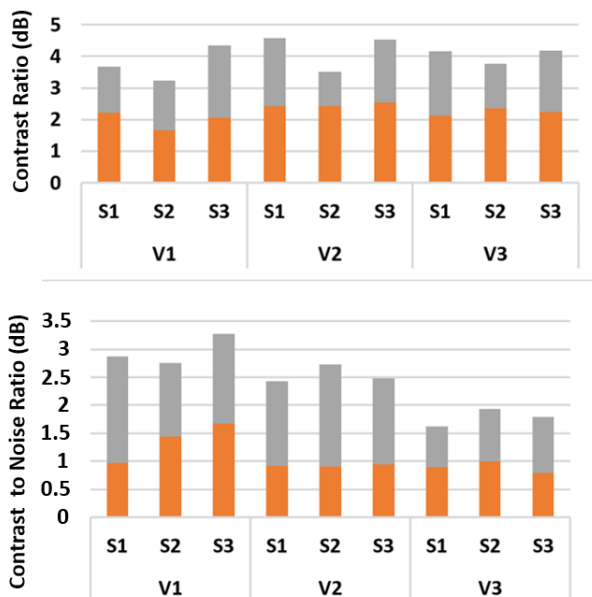


Figure 10: Quantitative average CNRs and CRs of the S-1, S-2, and S-3 diverging wave strategies over the three virtual sources configuration (C-1, C-2, and C-3). V1, V2, and V3 correspond to the three rotation speeds. The bars in orange/gray colors indicate the results without/with MoCo, respectively. Both gray and orange bars begin from the horizontal axis. For instance, the CNR results for S1/V1 are 1 and 2.9 without and with MoCo, respectively

Overall, the results confirmed that MoCo increased the CNR, CR, for each case. On average, the motion compensation algorithm increased, for the S-1, S-2, and S-3 strategies, the CNR of 1.28 ± 0.57 , 1.58 ± 0.74 , and 1.47 ± 0.68 dB, respectively, and the CR of 1.58 ± 0.74 , 1.64 ± 0.88 , and 2.2 ± 0.46 dB, respectively. In other words, the MoCo increased by a factor of 2 and 1.5 the CNR and CR, respectively. Another important result presented in this study is the comparison between the different rotation speeds. As expected, the images quality decreased when the disk rotated faster (Figure. 10). Moreover, the effect of the MoCo approach also decreased with faster rotation speed. A more important speed-related study is needed to highlight this limitation.

In this work, we used a conventional motion estimation algorithm based on the phase of the autocorrelation function, also called Tissue Doppler imaging. We expect the same bias/variance as conventional Tissue Doppler imaging

Only the axial component of the velocity was estimated and compensated [20], [22]. Even if the transverse motion have a little impact on PSF profile [20] this may be insufficient in case of fast/large displacement in the transverse directions. A significant improvement could be to estimate and compensate for the 3-D motion, using, for example, the TO strategies [35]–[37] or 3-D vector flow method [2], [23]. Finally, a rigid model-based motion estimation method has been used in this paper. However, the rigid hypothesis is not valid in the presence of cardiac tissue stretching and torsion. Another improvement could be the use of an affine model-based motion estimator.

V. CONCLUSIONS

In this manuscript, the use of the 3D HFR MoCo method with three different diverging wave strategies and three different configurations of virtual sources was analyzed in simulation and experiment. First of all a formalization of the location of the virtual source has been proposed according to different diverging wave strategies and opening angles. Then different scenarios were compared quantitatively by estimating the CNR and CR in simulation and in-vitro experiments. The results confirmed that MoCo increased both the CNR and the CR for each scenario. Overall, the MoCo algorithm increased on average the CNR/CR of $+3.2/8.3$ dB *in silico*, and of $+1.4/1.8$ dB *in vitro*, respectively

ACKNOWLEDGMENT

This work was supported by the LABEX PRIMES (ANR-11-LABX-0063) and the LABEX CELYA (ANR-10-LABX-0060) of the Université de Lyon, within the programme ‘Investissements d’Avenir’ (ANR-11-IDEX-0007), operated by the French National Research Agency (ANR). This material is based upon work done on the PLoT facility.

REFERENCES

- [1] M. S. Wigen *et al.*, “4-D Intracardiac Ultrasound Vector Flow Imaging—Feasibility and Comparison to Phase-Contrast MRI,” *IEEE Trans. Med. Imaging*, vol. 37, no. 12, pp. 2619–2629, Dec. 2018, doi: 10.1109/TMI.2018.2844552.
- [2] M. Correia, J. Provost, M. Tanter, and M. Pernot, “4D ultrafast ultrasound flow imaging: *in vivo* quantification of arterial volumetric flow rate in a single heartbeat,” *Phys. Med. Biol.*, vol. 61, no. 23, pp. L48–L61, Dec. 2016, doi: 10.1088/0031-9155/61/23/L48.
- [3] J. Sauvage *et al.*, “4D Functional Imaging of the Rat Brain Using a Large Aperture Row-Column Array,” *IEEE Trans. Med. Imaging*, vol. 39, no. 6, pp. 1884–1893, Jun. 2020, doi: 10.1109/TMI.2019.2959833.
- [4] J. Meunier, “Tissue motion assessment from 3D echographic speckle tracking,” *Phys. Med. Biol.*, vol. 43, no. 5, pp. 1241–1254, May 1998.
- [5] K. F. Kvåle *et al.*, “Detection of Tissue Fibrosis using Natural Mechanical Wave Velocity Estimation: Feasibility Study,” *Ultrasound Med. Biol.*, vol. 46, no. 9, pp. 2481–2492, Sep. 2020, doi: 10.1016/j.ultrasmedbio.2020.04.022.
- [6] C. Papadacci, E. A. Bunting, E. Y. Wan, P. Nauleau, and E. E. Konofagou, “3D Myocardial Elastography

- In Vivo,” *IEEE Trans. Med. Imaging*, vol. 36, no. 2, pp. 618–627, Feb. 2017, doi: 10.1109/TMI.2016.2623636.
- [7] S. Salles *et al.*, “3D Myocardial Mechanical Wave Measurements,” *JACC Cardiovasc. Imaging*, p. S1936878X20305957, Aug. 2020, doi: 10.1016/j.jcmg.2020.05.037.
- [8] G. Montaldo, M. Tanter, J. Bercoff, N. Benech, and M. Fink, “Coherent plane-wave compounding for very high frame rate ultrasonography and transient elastography,” *IEEE Trans. Ultrason. Ferroelectr. Freq. Control*, vol. 56, no. 3, pp. 489–506, Mar. 2009, doi: 10.1109/TUFFC.2009.1067.
- [9] C. Papadacci, M. Pernot, M. Couade, M. Fink, and M. Tanter, “High-contrast ultrafast imaging of the heart,” *IEEE Trans. Ultrason. Ferroelectr. Freq. Control*, vol. 61, no. 2, pp. 288–301, Feb. 2014, doi: 10.1109/TUFFC.2014.6722614.
- [10] L. Tong, H. Gao, and J. D’hooge, “Multi-transmit beam forming for fast cardiac imaging—a simulation study,” *IEEE Trans. Ultrason. Ferroelectr. Freq. Control*, vol. 60, no. 8, pp. 1719–1731, Aug. 2013, doi: 10.1109/TUFFC.2013.2753.
- [11] J. Provost *et al.*, “3D ultrafast ultrasound imaging *in vivo*,” *Phys. Med. Biol.*, vol. 59, no. 19, pp. L1–L13, Oct. 2014, doi: 10.1088/0031-9155/59/19/L1.
- [12] S. Salles, H. Liebgott, D. Garcia, and D. Vray, “Real time 3D US-tagging combined with 3D phasebased motion estimation,” *IEEE*, Jul. 2013, pp. 585–588. doi: 10.1109/ULTSYM.2013.0151.
- [13] E. Badescu *et al.*, “Comparison Between Multiline Transmission and Diverging Wave Imaging: Assessment of Image Quality and Motion Estimation Accuracy,” *IEEE Trans. Ultrason. Ferroelectr. Freq. Control*, vol. 66, no. 10, pp. 1560–1572, Oct. 2019, doi: 10.1109/TUFFC.2019.2925581.
- [14] J. C. Kirk, “Motion Compensation for Synthetic Aperture Radar,” *IEEE Trans. Aerosp. Electron. Syst.*, vol. AES-11, no. 3, pp. 338–348, May 1975, doi: 10.1109/TAES.1975.308083.
- [15] L. F. Nock and G. E. Trahey, “Synthetic receive aperture imaging with phase correction for motion and for tissue inhomogeneities. I. Basic principles,” *IEEE Trans. Ultrason. Ferroelectr. Freq. Control*, vol. 39, no. 4, pp. 489–495, Jul. 1992, doi: 10.1109/58.148539.
- [16] G. E. Trahey and L. F. Nock, “Synthetic receive aperture imaging with phase correction for motion and for tissue inhomogeneities. II. Effects of and correction for motion,” *IEEE Trans. Ultrason. Ferroelectr. Freq. Control*, vol. 39, no. 4, pp. 496–501, Jul. 1992, doi: 10.1109/58.148540.
- [17] K. S. Kim, J. S. Hwang, J. S. Jeong, and T. K. Song, “An Efficient Motion Estimation and Compensation Method for Ultrasound Synthetic Aperture Imaging,” *Ultrason. Imaging*, vol. 24, no. 2, pp. 81–99, Apr. 2002, doi: 10.1177/016173460202400202.
- [18] K. L. Gammelmark and J. A. Jensen, “2-D tissue motion compensation of synthetic transmit aperture images,” *IEEE Trans. Ultrason. Ferroelectr. Freq. Control*, vol. 61, no. 4, pp. 594–610, Apr. 2014, doi: 10.1109/TUFFC.2014.2948.
- [19] B. Denarie *et al.*, “Coherent Plane Wave Compounding for Very High Frame Rate Ultrasonography of Rapidly Moving Targets,” *IEEE Trans. Med. Imaging*, vol. 32, no. 7, pp. 1265–1276, Jul. 2013, doi: 10.1109/TMI.2013.2255310.
- [20] J. Poree, D. Posada, A. Hodzic, F. Tournoux, G. Cloutier, and D. Garcia, “High-Frame-Rate Echocardiography Using Coherent Compounding With Doppler-Based Motion-Compensation,” *IEEE Trans. Med. Imaging*, vol. 35, no. 7, pp. 1647–1657, Jul. 2016, doi: 10.1109/TMI.2016.2523346.
- [21] L. Nie, D. M. J. Cowell, T. M. Carpenter, J. R. McLaughlan, A. A. Cubukcu, and S. Freear, “High-Frame-Rate Contrast-Enhanced Echocardiography Using Diverging Waves: 2-D Motion Estimation and Compensation,” *IEEE Trans. Ultrason. Ferroelectr. Freq. Control*, vol. 66, no. 2, pp. 359–371, Feb. 2019, doi: 10.1109/TUFFC.2018.2887224.
- [22] Y. Chen, J. D’hooge, and J. Luo, “Doppler-Based Motion Compensation Strategies for 3-D Diverging Wave Compounding and Multiplane-Transmit Beamforming: A Simulation Study,” *IEEE Trans. Ultrason. Ferroelectr. Freq. Control*, vol. 65, no. 9, pp. 1631–1642, Sep. 2018, doi: 10.1109/TUFFC.2018.2851310.
- [23] Y. Chen, X. Luo, and J. Luo, “A 3D Motion Compensation Method for High Frame Rate Volumetric Ultrasound Imaging based on Velocity Vector Estimation: A Simulation Study,” in *2020 IEEE International Ultrasonics Symposium (IUS)*, Las Vegas, NV, USA: IEEE, Sep. 2020, pp. 1–4. doi: 10.1109/IUS46767.2020.9251770.
- [24] P. Joos *et al.*, “High-frame-rate 3-D echocardiography based on motion compensation: An *in vitro* evaluation,” in *2017 IEEE International Ultrasonics Symposium (IUS)*, Washington, DC, USA: IEEE, Sep. 2017, pp. 1–4. doi: 10.1109/ULTSYM.2017.8091671.
- [25] S. Salles, F. Varray, D. Garcia, B. Nicolas, and H. Liebgott, “Investigation on 3D high frame rate imaging with motion compensation (MoCo),” in *2019 IEEE International Ultrasonics Symposium (IUS)*, Glasgow, United Kingdom: IEEE, Oct. 2019, pp. 1274–1277. doi: 10.1109/ULTSYM.2019.8926273.
- [26] J. A. Jensen, “FIELD: A Program for Simulating Ultrasound Systems,” in *10TH NORDICBALTIC CONFERENCE ON BIOMEDICAL IMAGING, VOL. 4, SUPPLEMENT 1, PART 1:351–353*, 1996, pp. 351–353.
- [27] J. A. Jensen and N. B. Svendsen, “Calculation of pressure fields from arbitrarily shaped, apodized, and excited ultrasound transducers,” *IEEE Trans. Ultrason. Ferroelectr. Freq. Control*, vol. 39, no. 2, pp. 262–267, Mar. 1992, doi: 10.1109/58.139123.
- [28] L. Petrusca *et al.*, “Fast Volumetric Ultrasound B-Mode and Doppler Imaging with a New High-Channels Density Platform for Advanced 4D Cardiac Imaging/Therapy,” *Appl. Sci.*, vol. 8, no. 2, p. 200, Jan. 2018, doi: 10.3390/app8020200.
- [29] R. M. Souza, T. Q. Santos, D. P. Oliveira, R. M. Souza, A. V. Alvarenga, and R. P. B. Costa-Felix,

- “Standard operating procedure to prepare agar phantoms,” *J. Phys. Conf. Ser.*, vol. 733, p. 012044, Jul. 2016, doi: 10.1088/1742-6596/733/1/012044.
- [30] J. F. Deprez, E. Brusseau, C. Schmitt, G. Cloutier, and O. Basset, “3D estimation of soft biological tissue deformation from radio-frequency ultrasound volume acquisitions,” *Med. Image Anal.*, vol. 13, no. 1, pp. 116–127, Feb. 2009, doi: 10.1016/j.media.2008.07.003.
- [31] E. Badescu, D. Bujoreanu, L. Petrusca, D. Friboulet, and H. Liebgott, “Multi-line transmission for 3D ultrasound imaging: An experimental study,” in *2017 IEEE International Ultrasonics Symposium (IUS)*, Washington, DC: IEEE, Sep. 2017, pp. 1–4. doi: 10.1109/ULTSYM.2017.8091612.
- [32] D. Bera *et al.*, “Multiline 3D beamforming using micro-beamformed datasets for pediatric transesophageal echocardiography,” *Phys. Med. Biol.*, vol. 63, no. 7, p. 075015, Mar. 2018, doi: 10.1088/1361-6560/aab45e.
- [33] Y. Chen, L. Tong, A. Ortega, J. Luo, and J. D’hooge, “Feasibility of Multiplane-Transmit Beamforming for Real-Time Volumetric Cardiac Imaging: A Simulation Study,” *IEEE Trans. Ultrason. Ferroelectr. Freq. Control*, vol. 64, no. 4, pp. 648–659, Apr. 2017, doi: 10.1109/TUFFC.2017.2651498.
- [34] I. K. H. Tsang, B. Y. S. Yiu, and A. C. H. Yu, “A least-squares vector flow estimator for synthetic aperture imaging,” in *2009 IEEE International Ultrasonics Symposium*, Rome, Italy: IEEE, Sep. 2009, pp. 1387–1390. doi: 10.1109/ULTSYM.2009.5441624.
- [35] M. J. Pihl, M. B. Stuart, B. G. Tomov, M. F. Rasmussen, and J. A. Jensen, “A transverse oscillation approach for estimation of three-dimensional velocity vectors, part II: experimental validation,” *IEEE Trans. Ultrason. Ferroelectr. Freq. Control*, vol. 61, no. 10, pp. 1608–1618, Oct. 2014, doi: 10.1109/TUFFC.2013.006238.
- [36] S. Salles, A. J. Y. Chee, D. Garcia, A. C. H. Yu, D. Vray, and H. Liebgott, “2-D arterial wall motion imaging using ultrafast ultrasound and transverse oscillations,” *IEEE Trans. Ultrason. Ferroelectr. Freq. Control*, vol. 62, no. 6, pp. 1047–1058, Jun. 2015, doi: 10.1109/TUFFC.2014.006910.
- [37] S. Salles, H. Liebgott, D. Garcia, and D. Vray, “Full 3-D transverse oscillations: a method for tissue motion estimation,” *IEEE Trans. Ultrason. Ferroelectr. Freq. Control*, vol. 62, no. 8, pp. 1473–1485, Aug. 2015, doi: 10.1109/TUFFC.2015.007050.